Journal of the Optical Society of America B
OPTICAL PHYSICS

Realizing ultra-bandwidth cross-polarization conversion by a double-layer metasurface

Yupeng Li,[1] Haifeng Zhang,[1,2,*] Tong Yang,[1] Tangyi Sun,[1] and Li Zeng[1]

[1]College of Electronic and Optical Engineering & College of Microelectronics, Nanjing University of Posts and Telecommunications, Nanjing, Jiangsu Province 210023, China
[2]State Key Laboratory of Millimeter Waves of Southeast University, Nanjing 210096, China
*Corresponding author: hanlor@163.com

Received 10 July 2020; revised 7 September 2020; accepted 22 September 2020; posted 24 September 2020 (Doc. ID 402479); published 3 November 2020

In this paper, a double-layer structure of ultra-bandwidth cross-polarization converter (PC) has been devised in line with the rationale of the metasurface. The project can bring about a superior 90° conversion effect of the incident wave when it is perpendicularly incident. This PC is an improvement and majorization of the single-layer PC with a bowknot surface structure, which can hit the mark of improving the polarization conversion ratio in the low frequencies and enlarging the bandwidth. In this article, not only is the basic principle of polarization conversion examined but also the parameters are discussed. In addition, points of view such as incidence angle and current are utilized for analysis. Ultimately, the cross-polarization conversion can be achieved in the range of 0.63–1.50 THz, whose relative bandwidth is 81.7% and bandwidth is 0.87 THz. The proposed design may be worth applying in radar, communication, and imaging technologies.

https://doi.org/10.1364/JOSAB.402479

1. INTRODUCTION

Polarization refers to the phenomenon where the direction and amplitude of the electric field intensity of an electromagnetic (EM) wave in space can be changed in the wake of time [1–6]. Supposing that such a change possesses a specific trajectory, the EM wave is called a polarized EM wave [7–12]. On the basis of the shape of the trail, we can classify polarized EM waves into three categories, which are linear, circular, and elliptically polarized EM waves [13–17]. It should be emphasized that among them, the cross-polarization converter (PC) provides the function of switching linearly polarized EM waves between two polarization modalities.

Metasurfaces are a branch of metamaterials that have the merits of miniaturization and plate integration [18–23]. From the structure point of view, the metasurface is a sort of two-dimensional array composed of metamaterial units. In terms of function, the metasurface is used in the propagation of the polarized EM waves in common. More specifically, when the metasurface is situated in two types of medium, it can control the direction of EM waves and realize the functions of beam shaping, radar scanning, and so on [24–28]. Since metasurfaces overcome the shortcomings of conventional materials, such as bulky volume and exorbitant loss, they have been paid close attention in recent years. Consequently, the appearance of metasurfaces promotes the development of the PC tremendously [29–33].

Because the significant role of the metasurface is becoming increasingly prominent, researchers are pursuing it vigorously. Hence, a great number of valuable research outcomes and techniques have come to the fore. For instance, two single-layer PCs with double V-shaped and trapezoid surface structures [34,35] were developed separately in 2015 and 2017. With regard to a dual V-shape PC, the relative bandwidth (RB) of 77.1% can be actualized at 12.40–27.96 GHz. In comparison, the trapezoid PC can fit the operating band to a low frequency which has a wider range of applications, while being able to approach the same RB as above to a great extent.

A great number of PCs are similar to these single-layer structures mentioned above, but most of them lose the ability to obtain better conversion effect indirectly due to the simplicity of the structure. However, in a paper written by Jia *et al*. [36], the authors compared the different conversion effects when the PCs they designed were with a single layer and a double layer. Through the analysis, it is distinct and apparent that the double-layer structure can optimize not only the polarization conversion ratio (PCR) but also the operating band of the PC to a certain degree. Specifically, the double-layer structure is closer to 180 deg in terms of phase difference, and the PCR is elevated at 29–34 GHz. Eventually, the design can achieve more than 95% polarization conversion efficiency in 7.8–34.7 GHz.

In addition, summary and comparison of polarization converters are shown in Table 1. First, in 2018, a single-layer nested

Table 1. Comparison with Other Polarization Converters

Ref.	Band	Polarization Mode	Structure
[37]	0.65–1.58 THz (PCR > 80%)	Reflective PC	Single layer
[38]	4.67 and 8.51 GHz	Transmissive PC	Single layer
[39]	9.1–16.5 GHz 17.4–18.9 GHz 20.0–25.4 GHz	Reflective PC	Double layers
Present study	0.63–1.50 THz ((PCR > 90%))	Reflective PC	Double layers

ring PC which can bring out more than 80% PCR within 0.65–1.58 THz was designed by Zhao *et al.* [37]. What can be discovered is that this single-layer PC can achieve the function of reflective polarization conversion in 0.65–1.58 THz under the standard of PCR > 80%. Obviously, this efficiency index is no longer applicable to the current electromagnetic development needs. In the same year, this research team further proposed a novel planar chiral metamaterial [38], which can realize the transmissive polarization convention at 4.67 GHz and 8.51 GHz. Similar to the present study, Liu *et al.* [39] realized the purpose of generating polarization conversion in three separate narrow bands through the design of the double-layer structure in 2016. Possessing a triple band is its merit, but the lack of enough relative bandwidth in each band is also its disadvantage.

Through the comprehension of the above documents, some inspiration about how to ameliorate the shortages of previously devised bowknot PCs was arrived at. Similarly, the proposed design has been improved by adding the second-layer structure. Eventually, the RB of this product is raised from 46.8% to 81.7%. In addition, the PC can come true more than 90% of PCR in the working band of 0.63–1.50 THz.

2. THEORETICAL MODEL

As for the design of the model, the HFSS is a commercial software used in 3D EM simulation. Figure 1(a) provides the unit topology of the devised double-layer cross-PC, which is displayed in a perspective state intentionally at the moment of drawing to facilitate the comprehending of the structure. It can be seen from Fig. 1(a) plainly, from the bottom to the top, that the product consists of the metal plate on the lowest, the first

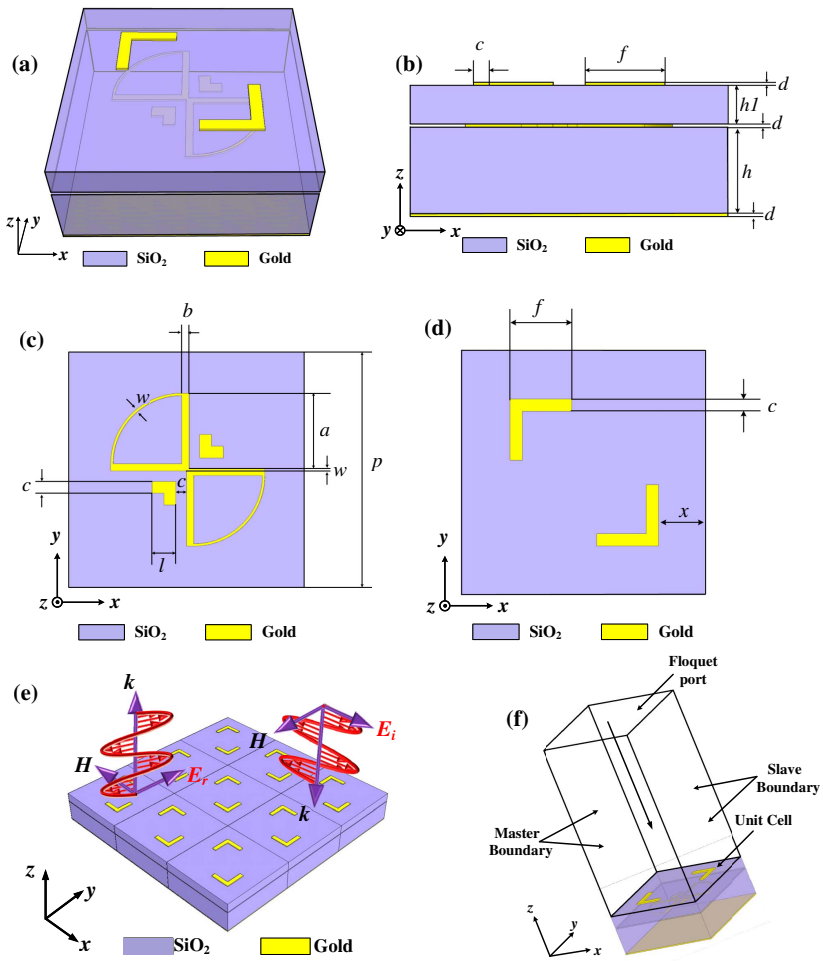

Fig. 1. Structural graphs of the proposed double-layer PC: (a) the perspective stereogram of the unit structure, (b) the side view of the unit cell, (c) the abridged picture of the first layer, (d) the diagrammatic sketch of the second layer, (e) array diagram (3 × 3) of the periodic arrangement, and (f) schematic diagram of boundary conditions.

Table 2. Parameters of the Design

Parameters	*a*	*b*	*c*	*d*	*F*
Value (μm)	33	3	5	0.03	25
Parameters	*l*	*w*	*p*	*x*	*h*
Value (μm)	10	1	100	20	27
Parameters	*h*1				
Value (μm)	12				

dielectric layer with a bowknot unit above the bottom layer, as well as the second dielectric layer, possessing the L-shaped units, on the topmost. Figure 1(b) is the side view of the structure. This diagrammatic sketch reveals some information. The thickness of the metal is d and the dielectric substrates in different positions display diverse thicknesses whose values are $h = 27$ μm and $h1 = 12$ μm, respectively.

Counting from bottom to top, the vertical views of the first and the second layers are shown in Figs. 1(c) and 1(d). The surface unit of the first layer resembles a bowknot which consists of a pair of center-symmetrical fans and a couple of small L-shaped structures equaled from both sides of the fans. However, the surface structure of the second layer is relatively simpler than that of the first layer. They are a pair of large L-shaped structures whose positions are symmetrical along the center with the same size and form. Ultimately, the units are arrayed periodically, and they will be combined into a metasurface which is provided with the cross-polarization conversion function as shown in Fig. 1(e).

Regarding materials, we utilized two types. The metal portions are realized by gold, whose electrical conductivity is 4.561×10^7 s/m. Furthermore, the dielectric substrate is a kind of material called SiO_2 with a dielectric constant of 4.0 [40]. And other specifc values of the parameters are shown in Table 2. Concerning the analog simulation of this model, the boundless period can be obtained by setting the boundary condition to Master–Slave as illustrated in Fig. 1(f). Meanwhile, the Floquet port is installed on the top so that x-polarized waves can be perpendicularly incident.

3. ANALYSIS AND DISCUSSION

Due to the adjunction of the bottom gold plate, almost all EM waves are not able to engender the circumstances of transmission. Therefore, concerning the situation of reflection can be taken into account as much as possible in the following discussion. In the first place, r_{xx} and r_{yx} are defined as the co-polarization reflection coefficient and cross-polarization reflection coefficient, respectively, when the incident wave is following the x axis. So, the formula of the PCR can be expressed as

$$\mathrm{PCR} = \frac{r_{yx}^2}{r_{yx}^2 + r_{xx}^2}. \tag{1}$$

When r_{yx} is close to 1 and r_{xx} approaches 0, an excellent value of PCR will be attained. Second, the reflection coefficient is represented as r_{uu} when the electric field directions of incidence and emitted EM waves are both along the u axis, and the reflection coefficient called r_{vv} is defined in the same way. Meanwhile,

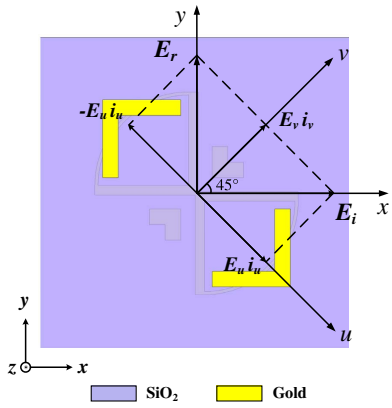

Fig. 2. Schematic diagram of EM waves turning from the x to the y axis.

we can gain the corresponding phases which are φ_{uu} and φ_{vv}, individually. Thus, the conditions which the cross-polarization conversion should meet are that not only r_{uu} and r_{vv} are equal but also the phase difference ($\Delta\varphi = \varphi_{uu} - \varphi_{vv}$) is 180 deg approximately.

However, the more concrete reasons why we should discuss conditions like those above are recounted as follows. In the plane coordinate system, in addition to the x and y axes, we can also define the u and v axes. When the EM wave comes in along the x axis, the electric field vector of it can be expressed as $\boldsymbol{E_i} = E_x \boldsymbol{i_x}$, which is provided with the components called $\boldsymbol{E_u i_u}$ and $\boldsymbol{E_v i_v}$ in the u and v axes, respectively. In other words, $\boldsymbol{E_i} = \boldsymbol{E_v i_v} + \boldsymbol{E_u i_u}$. Similarly, the electric field vector $\boldsymbol{E_r}$ of the reflected EM wave revealed in Fig. 2 can be described as the following formula:

$$\boldsymbol{E_r} = \begin{pmatrix} \boldsymbol{i_u} & \boldsymbol{i_v} \end{pmatrix} \begin{pmatrix} r_{uu} & r_{uv} \\ r_{vu} & r_{vv} \end{pmatrix} \begin{pmatrix} \boldsymbol{E_u} \\ \boldsymbol{E_v} \end{pmatrix}, \tag{2}$$

where i_u and i_v are the conventional letters of the unit vectors, and r_{uu} and r_{vv} represent the co-polarization reflection coefficients when the electric field directions of incident EM waves are following the u and v axes, respectively. Furthermore, the cross-polarization reflection coefficients whose values are equal to 0 are expressed as r_{vu} and r_{uv} (the reason why r_{vu} and $r_{uv} = 0$ is that the structure of the design is symmetrical in the u and v axes). Expanding the above formula for further calculation, the following result can be gained:

$$\boldsymbol{E_r} = \boldsymbol{E_x} \cos(45°)\left(r_{uu}\boldsymbol{i_u} + r_{vv}\boldsymbol{i_v}\right), \tag{3}$$

where $r_{uu} = |r_{uu}|e^{j\varphi u}$ and $r_{vv} = |r_{vv}|e^{j\varphi v}$. It is noteworthy that if the conditions $|r_{uu}| = |r_{vv}| = 1$ and $\Delta\varphi = \pi + 2n\pi$ (n is an integer) are met, the $\boldsymbol{E_r}$ can be simplified by calculation as

$$\boldsymbol{E_r} = \boldsymbol{E_x} \cos(45°)\boldsymbol{e}^{j\varphi v}(\boldsymbol{i_u} + \boldsymbol{e}^{j\Delta\varphi}\boldsymbol{i_v}) = -\boldsymbol{E_x}\boldsymbol{e}^{j\varphi v}\boldsymbol{i_y}. \tag{4}$$

This proves that the reflected EM wave will deflect by 90 deg, causing the broadcast direction of the polarization to shift from the x axis to the y axis. Eventually, the effect of cross-polarization conversion has emerged.

Academically, the part of the PCR greater than 0.9 generally defaults to the scope of operation, so hereinafter, the reference

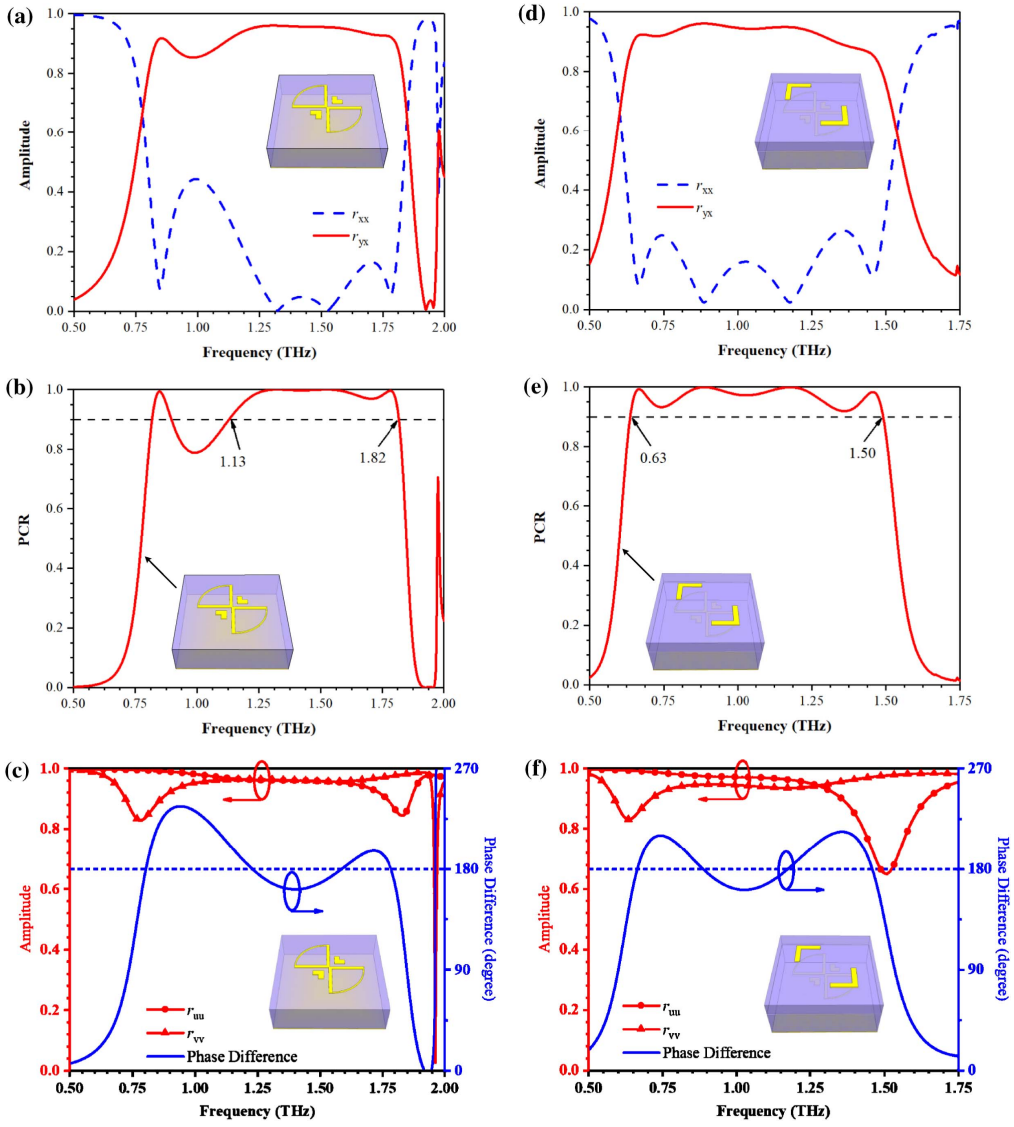

Fig. 3. Schematic diagrams of the single-layer structure: (a) refection amplitude curves of EM waves incident along the x axis, (b) refined curve of the PCR, and (c) amplitude and phase difference curves of EM waves moving along u and v axes. Schematic diagrams of the double-layer PC: (d) simulated reflection amplitude, (e) the curve of the PCR, and (f) phase difference and amplitude curves.

line of PCR = 0.9 will be marked in portrayals of the PCR curve. When the PCR curve exists above the baseline of 0.9 continuously in a wide range, the intersection points between the authentic curve and the baseline of the PCR are artificially called f_L and f_H, which are located in the lower and higher frequencies, respectively. As described above, more specific bandwidth and RB formulas which are written as Δf and $ffoc$ can be expressed as $\Delta f = f_H - f_L$ and $ffoc = 2\Delta f/(f_H + f_L)$.

To provide context for the double-layer PC, the single-layer structure will be introduced for a comparative discussion. Figures 3(a) and 3(d) represent the reflection amplitude vividly when the EM wave is vertically incident along the x axis. The red and blue curves indicate r_{yx} and r_{xx}, respectively. As shown in Fig. 3(a), r_{yx} ascend swiftly from below 0.2 to above 0.8, and the trend of r_{xx} is just the opposite. But it is worth noting that r_{xx} is so high that it outstrips 0.4 in the vicinity of 1 THz. That is the reason why the curve of the PCR possesses a deterioration value lower than 0.9 at the low frequency as displayed in Fig. 3(b), resulting in a design where RB is 46.8% operating merely in the 1.13–1.82 THz. It is thus clear that certain inadequacies still exist in the single-layer PC. In particular, there is a great room to ameliorate in the relevant indicators such as the PCR in the low frequency, RB, and so on. Therefore, aiming at the discovered problems and combining with experience and related thesis, the improved solution of adding the second-layer structure is adopted. Compared with Fig. 3(a), the change trends of r_{yx} and r_{xx} are similar to those of the single-layer design. However, the significant difference is that the band whose amplitude meets the condition of polarization conversion is shifted toward the low frequency, and the curves have been ameliorated. In particular, the first halves of r_{yx} and r_{xx} do better in terms of approaching 1 and 0, respectively, as displayed in Fig. 3(d). In addition, the invention possesses four frequency points, which are 0.665 THz, 0.891 THz, 1.175 THz, and 1.459 THz, and

they approach mutually to form a working band with a broadband effect. Then, 81.7% of the RB and the PCR which is more than 90% can be acquired in the band of 0.63–1.50 THz, as shown in Fig. 3(e).

Furthermore, according to the above theories, it can be further discussed when the EM waves are incident along the u and v axes, respectively. At the working band of the single-layer structure, the two red curves representing r_{uu} and r_{vv}, fit each other, and the phase difference also fluctuates around 180 deg. However, there are still some deficiencies that affected the effectiveness of the polarization conversion as mentioned before. As shown in Fig. 3(c), the actual phase difference is significantly different from 180 deg at 1 THz or thereabouts, which has been improved under the action of the double-layer structure, as shown in Fig. 3(f).

In order to better expound the physical mechanization of the proposed ultra-bandwidth cross-PC, we have discussed the current distribution. The curves in Figs. 3(d) and 3(e) reveal that the PC possesses four resonance frequencies, of which 0.891 THz and 1.175 THz are relatively outstanding. So, the current distribution at 0.891 THz and 1.175 THz will be explained in detail, and the rest can be deduced by analogy. The current trend and equivalent current are represented as black and red arrows, respectively, in Fig. 4. Specifically, as expressed in Fig. 4(b), the currents on each branch can ultimately be equivalent to arrows 3 and 4. In addition, the currents in the metal plate can be disassembled into arrows 5 and 6, as shown in Fig. 4(c). It is obvious that the currents in the middle and bottom layers are in opposite directions (3 contraries to 6 and 4 reverses to 5). So, the circulating currents are formed between the two layers while the magnetic resonances are generated. However, the existence of magnetic resonance stimulates the generation of the induced magnetic fields, and the parts of the magnetic fields which are parallel to the electric field will engender polarization conversion. In like manner, the correspondence between Figs. 4(a) and 4(b) can be discussed using the above train of thought. Although the current intensity of the top layer is feeble, it also plays an auxiliary role for the middle layer, which eventually achieves the effect of enhancing polarization conversion.

Nevertheless, the current distributions of 1.175 THz are slightly different from 0.891 THz. The directions of top layer currents are no longer the same as those of the middle layer while they are in the opposite directions, as displayed in Figs. 4(d) and 4(e). The equivalent currents 1 and 3 are in contrary directions and so are 2 and 4. So, more than one circulation between the two layers has emerged. In addition, taking the metal plate as the main part, it can be discovered that the currents on the metal plate can also seek out the corresponding opposite currents in the upper two layers. For instance, 5 corresponds to 4, 7, and 9 responses to 2, and so on. The same as above, due to the interactions of currents on different layers, the magnetic fields of different strengths are generated. Eventually, the component of the magnetic field which is parallel to the electric field will touch off the result of the polarization conversion. To sum up, through the detailed comparisons between Figs. 3(a)–3(f), it is clear that the addition of the second-layer structure can not only optimize the reflection amplitude curves but also make the phase difference closer to 180 deg. Further discussions can be

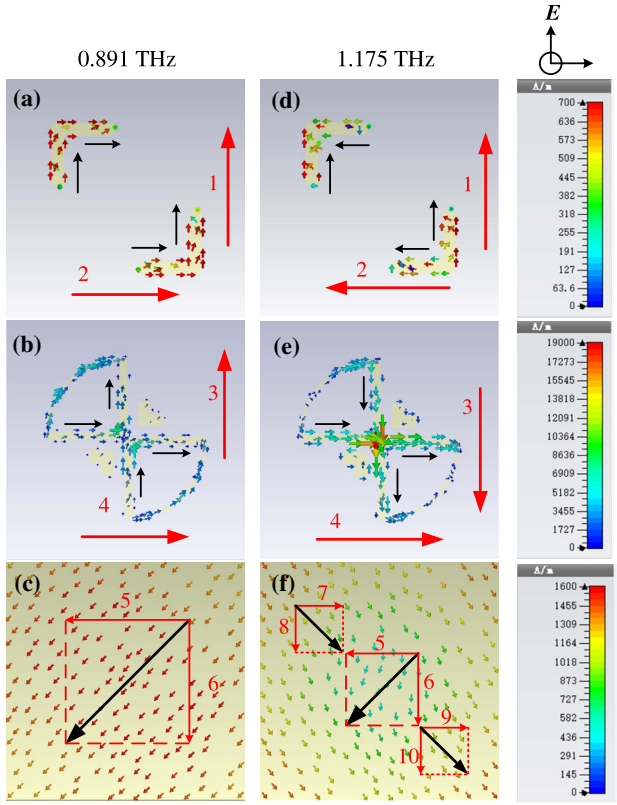

Fig. 4. Analysis diagrams of current distributions at 0.891 THz and 1.175 THz, respectively: (a) and (d) are in the topmost layer, (b) and (e) are in the middle layer, and (c) and (f) are in the lowest floor.

attributed to the increase of the magnetic resonances. With the addition of the second-layer structure, more circulating currents are generated between the structures; thus, the magnetic resonances are enhanced, and the polarization conversion efficiency is correspondingly improved. All of these are significant reasons to improve polarization conversion efficiency.

Furthermore, the comprehensive analysis of the electric field and phase at 0.891 THz is supplemented and investigated in Fig. 5, which indicates the local region of the electric field and the corresponding phase distribution. We can see from Figs. 5(a) and 5(b) that the components of $\boldsymbol{E_x}$ are located in zone 1 and zone 2, possessing a phase difference of π, causing a destructive interference so that this component is suppressed in the far field. In contrast, the local location of $\boldsymbol{E_y}$ in zone 3 maintains the same phase, as shown in Figs. 5(c) and 5(d), which leads to constructive interference and radiation enhancement phenomena in the far field. Therefore, the cross-polarization conversion is effectively implemented from x polarization to y polarization.

The sensitivity of the proposed design to the angular deflection of incident EM waves is described clearly as displayed in Fig. 6. The purple dashed line marks the range of the PCR which is above 0.9 specifically. The transformation of color indicates the variation and trend of the PCR which is affected by the incidence angle of EM waves. Figure 6(a) shows the relationship between the PCR and the incident angle when the proposed PC is merely a single-layer structure. Basically, the PCR at 0.82 THz does not produce large fluctuations with the change of incident angle. However, in the band of 1.13–1.82 THz, the deteriorated

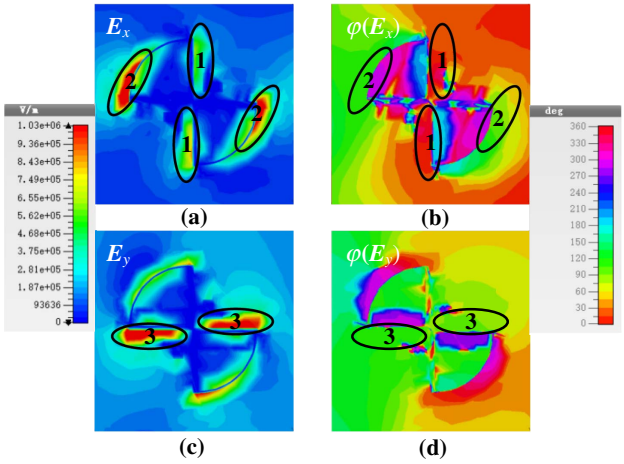

Fig. 5. Analysis diagrams of electric field and phase distributions at 0.891 THz: (a) and (b) correspond to $\boldsymbol{E_x}$ and $\varphi(\boldsymbol{E_x})$, (c) and (d) correspond to $\boldsymbol{E_y}$ and $\varphi(\boldsymbol{E_y})$.

frequency point emerges for the first time at 1.75 THz when the incident angle is 5 deg approximately. Subsequently, when the incident angle is deflected to 10 deg, the second degraded frequency point appears at 1.56 THz. Although there is no frequency point depression in the 1.13–1.56 THz range, the operable range is also shrinking swiftly.

After being ameliorated by adding a double-layer structure, the sensitivity of the PC to the incident angle has changed, as shown in Fig. 6(b). Specifically speaking, the preferable index can be maintained in the operating band when the incidence angle is lower than 23 deg. However, the PCR around 0.75 THz and 1.38 THz will exacerbate as the incidence angle magnifies; meanwhile, the range of deterioration shifts to the intermediate frequency. Finally, two towering polarization conversion peaks form at 0.67 THz and 1.06 THz, which means the excellent PCR still can be retained as before at these two points. To sum up, the method of adding the second-layer structure can be wielded to optimize the sensitivity of the incident angle for this design. The double-layer design can accommodate a larger angle of incidence deflection, which means that the PC maintains an efficient polarization conversion at a large angle of incidence.

The above analog computation results are based on the mode polarization of TE. Nevertheless, we also simulated the double-layer PC in the TM polarization mode. Through analysis of the outcomes in the two modes, we found that due to the structural symmetry which is along the diagonal, whether the TE or TM mode, the calculated data all agree with Fig. 6(b). Therefore, the discussion on the TM mode will not be repeated.

Further, the influence of the structural parameters on the operating performance is discussed in detail. The parameters h and w which belong to the middle layer represent the thickness of the dielectric layer and the ring width of the bowknot, respectively. Moreover, the parameters f and $h1$ of the topmost layer indicate the length of the L-shape structure and the thickness of the dielectric layer, respectively. Figure 7(a) demonstrates the fact that the increase of w creates a deteriorating effect on the PCR at a high frequency. Specifically, the PCR at the frequency point of 1.37 THz worsens from 0.92 to 0.60 when the value of w is raised from 1 μm to 9 μm. The reason why this phenomenon occurs is mainly that the frequency points at 1.18 THz and 1.46 THz have different degrees of redshift and blueshift, respectively, as shown in Fig. 7(e). As the above two frequency points are far away from each other, the broadband effect originally caused by the clustering of points at high frequencies is weakened gradually. Eventually, an unexpected "gully" of the PCR has emerged.

However, as shown in Figs. 7(b) and 7(c), no matter the change of h or $h1$, the influence on the PCR possesses a common characteristic; that is, in pace with the rise of the value of parameters, the PCR rises gradually at low frequency and reverses at high frequency. This changing trend is embodied more apparently on the parameter h. When digging deeper into how the parameter h affects the PCR, we found that with the value of h magnified, two frequency points originally located at 1.04 THz and 1.29 THz both produce redshifts to a certain extent as shown in Fig. 7(f). When $h = 31$ μm, two original

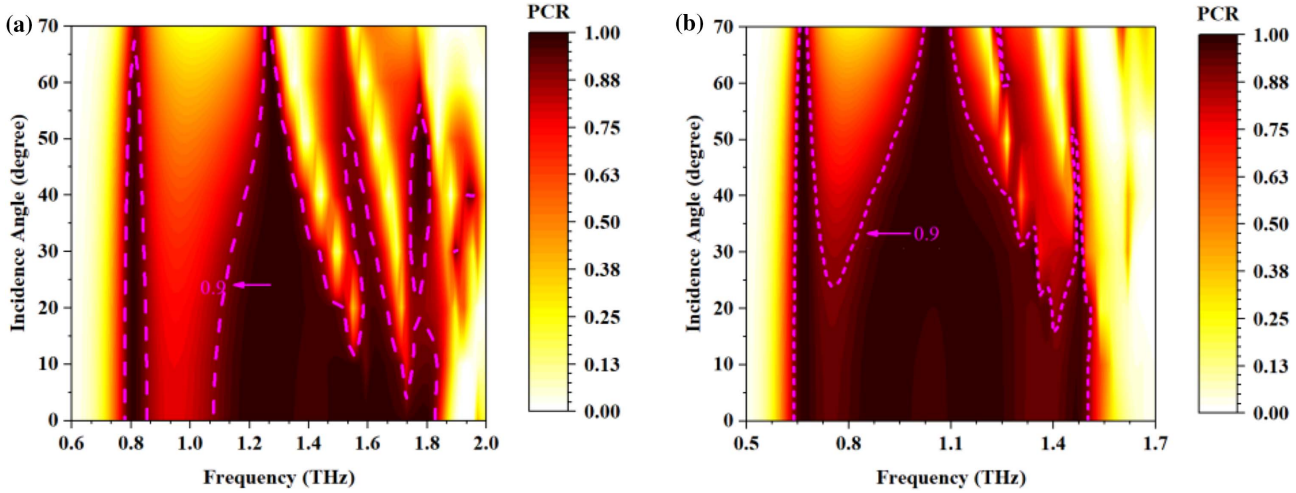

Fig. 6. Graph of the PCR induced by incidence EM waves at different angles: (a) for the single-layer structure and (b) for the double-layer structure.

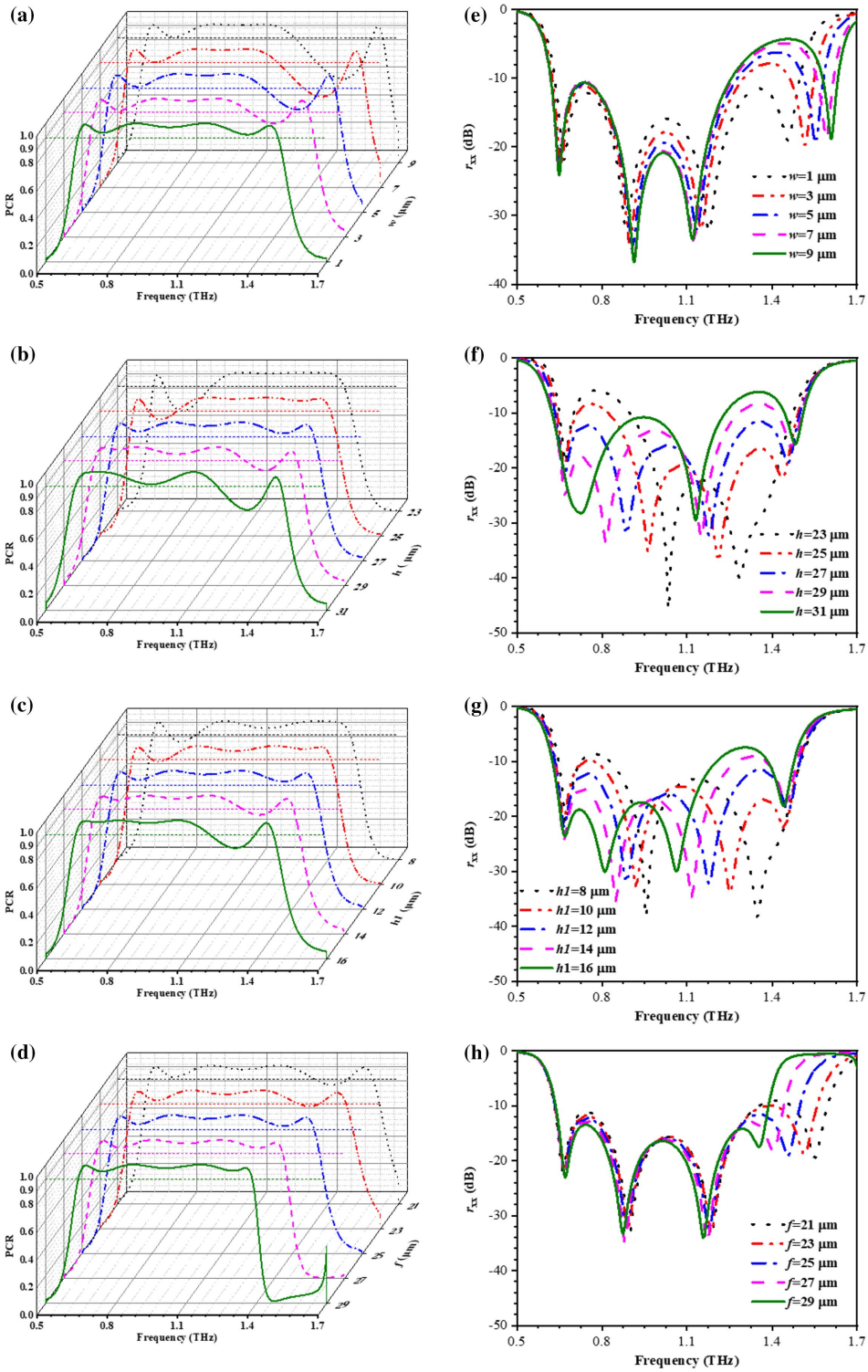

Fig. 7. Multiple scan curves of the PCR and r_{xx} with different parameters: (a), (e) the values of w are from 1 μm to 9 μm; (b), (f) the values of h change from 23 μm to 31 μm; (c), (g) the range of $h1$ is from 8 μm to 16 μm; and (d), (h) the values of f range from 21 μm to 29 μm.

points situated at 0.67 THz and 1.04 THz have been amalgamated into one frequency point, and at 1.48 THz a new frequency point appeared. Moreover, the same can be said for the analysis of parameter $h1$. For this duration, the PCR can attain a demand of greater than 0.9 in the operating band when $h = 27$ μm and $h1 = 12$ μm.

Furthermore, the descent of parameter f expands the bandwidth while deteriorating the PCR at high frequency to some extent. It can be discovered from Fig. 7(d) that the PCR curve at high frequency drops below 0.9 when the band is broadened from 0.63–1.38 THz to 0.63–1.59 THz. Also, the specific analysis of Fig. 7(h) is similar to the above discussion of

parameter w. On account of the eminent PCR and the broad working band being all we need, looking at it comprehensively, $f = 25$ μm is chosen as the superior value.

Ultimately, certain suggestions and methods for the experiment will also be proposed. In the experimental environment, two antennas, which represent the signal source and receiver, can be set on two rotatable perpendicular arms and linked to vector network analysis instruments individually. Then the sample is fastened in a place ahead of the antennas. Concurrently, we ensure the three are on the same horizontal height. In this case, by controlling the rotation angle of the perpendicular arm where the receiving antenna is located, different polarization reflection coefficients can be reached (rotation of 0 and 90 deg corresponds to the co-polarized and cross-polarized reflection coefficients, respectively). When the two antennas move at a certain angle with the sample as the center of the circle, the operating results under different incident angles can be obtained.

4. CONCLUSION

A metasurface with a double-layer structure is put forward in this paper. In this article, we utilize the method of adding the second-layer structure to improve the PC of the single-layer structure, and various analysis methods are used to describe the principles, incentive patterns, and other aspects. In addition, the partial data of the single-layer and double-layer PCs are compared, which authenticates that adding the second layer does ameliorate the related indices of the proposed PC to some extent. Ultimately, a PCR of more than 90% can be attained in the operating band of 0.63–1.50 THz by the proposed design whose RB is 81.7%.

Funding. Jiangsu Overseas Visiting Scholar Program for the University Prominent Young Middle-aged Teachers and Presidents; Open Research Program in China's State Key Laboratory of Millimeter Waves (K201927).

Disclosures. The authors declare no conflicts of interest.

REFERENCES

1. L. Martinez-Lopez, J. Rodriguez-Cuevas, J. I. Martinez-Lopez, and A. E. Martynyuk, "A multilayer circular polarizer based on bisected split-ring frequency selective surfaces," IEEE Antennas Wireless Propag. Lett. **13**, 153–156 (2014).
2. Y. F. Li, J. Q. Zhang, S. B. Qu, J. F. Wang, L. Zheng, Y. Q. Pang, Z. Xu, and A. X. Zhang, "Achieving wide-band linear-to-circular polarization conversion using ultra-thin bi-layered metasurfaces," J. Appl. Phys. **117**, 044501 (2015).
3. E. Doumanis, G. Goussetis, J. L. G. Tornero, R. Cahill, and V. F. Fusco, "Anisotropic impedance surfaces for linear to circular polarization conversion," IEEE Trans. Antennas Propag. **60**, 212–219 (2012).
4. L. Martinez-Lopez, J. Rodriguez-Cuevas, J. I. Martinez-Lopez, and A. E. Martynyuk, "Cascaded circular-polarisation-selective surface based on bisected split rings," Electron. Lett. **50**, 1335–1336 (2014).
5. Y. Z. Cheng, C. Fang, X. S. Mao, R. Z. Gong, and L. Wu, "Design of an ultrabroadband and high-efficiency reflective linear polarization convertor at optical frequency," IEEE Photonics J. **8**, 7805509 (2016).
6. Z. Z. Cheng and Y. Z. Cheng, "A multi-functional polarization convertor based on chiral metamaterial for terahertz waves," Opt. Commun. **435**, 178–182 (2019).
7. M. Mutlu and E. Ozbay, "A transparent 90° polarization rotator by combining chirality and electromagnetic wave tunneling," Appl. Phys. Lett. **100**, 051909 (2012).
8. O. Altintas, E. Unal, O. Akgol, M. Karaaslan, F. Karadag, and C. Sabah, "Design of a wide band metasurface as a linear to circular polarization converter," Mod. Phys. Lett. B **31**, 509–594 (2017).
9. J. Y. Tang, Z. Y. Xiao, K. K. Xu, X. L. Ma, D. J. Liu, and Z. H. Wang, "Cross polarization conversion based on a new chiral spiral slot structure in THz region," Opt. Quantum Electron. **48**, 111 (2016).
10. J. M. Hao and L. Zhou, "Electromagnetic wave scatterings by anisotropic metamaterials: generalized 4×4 transfer-matrix method," Phys. Rev. B **77**, 094201 (2008).
11. J. C. Zhao and Y. Z. Cheng, "A high-efficiency and broadband reflective 90 degrees linear polarization rotator based on anisotropic metamaterial," Appl. Phys. B **122**, 255 (2016).
12. Y. Z. Cheng, W. Y. Li, and X. S. Mao, "Triple-band polarization angle independent 90° polarization rotator based on fermat's spiral structure planar chiral metamaterial," Prog. Electromag. Res. **165**, 35–45 (2019).
13. W. Wang, Z. Y. Guo, R. Z. Li, J. R. Zhang, A. J. Zhang, Y. Li, Y. Liu, X. S. Wang, and S. L. Qu, "L-shaped metasurface for both the linear and circular polarization conversions," J. Opt. **17**, 065103 (2015).
14. Q. Zheng, C. J. Guo, and J. Ding, "Wideband metasurface-based reflective polarization converter for linear-to-linear and linear-to-circular polarization conversion," IEEE Antennas Wireless Propag. Lett. **17**, 1459–1463 (2018).
15. Y. Z. Cheng, J. P. Fan, H. Luo, and F. Chen, "Dual-band and high-efficiency circular polarization convertor based on anisotropic metamaterial," IEEE Access **99**, 7615–7621 (2019).
16. Y. Z. Cheng, J. P. Fan, H. Luo, F. Chen, N. X. Feng, X. S. Mao, and R. Z. Gong, "Dual-band and high-efficiency circular polarization conversion via asymmetric transmission with anisotropic metamaterial in the terahertz region," Opt. Mater. Express **9**, 1365–1376 (2019).
17. Y. Zhao and A. Alu, "Manipulating light polarization with ultrathin plasmonic metasurfaces," Phys. Rev. B **84**, 205428 (2011).
18. S. Sun, Q. He, J. Hao, S. Xiao, and L. Zhou, "Electromagnetic metasurfaces: physics and applications," Adv. Opt. Photonics **11**, 380–479 (2019).
19. S. Xiao, J. Wang, F. Liu, S. Zhang, X. Yin, and J. Li, "Spin-dependent optics with metasurfaces," Nanophotonics **6**, 215–234 (2017).
20. C. Qu, S. Ma, J. Hao, M. Qiu, X. Li, S. Xiao, Z. Miao, N. Dai, Q. He, S. Sun, and L. Zhou, "Tailor the functionalities of metasurfaces based on a complete phase diagram," Phys. Rev. Lett. **115**, 235503 (2015).
21. S. Sun, Q. He, S. Xiao, Q. Xu, X. Li, and L. Zhou, "Gradient-index meta-surfaces as a bridge linking propagating waves and surface waves," Nat. Mater. **11**, 426–431 (2012).
22. Y. N. Jiang, L. Wang, J. Wang, C. Akwuruoha, and W. P. Cao, "Ultra-wideband high-efficiency reflective linear-to-circular polarization converter based on metasurface at terahertz frequencies," Opt. Express **25**, 27616–27623 (2017).
23. H. Y. Sun, C. Q. Gu, X. L. Chen, Z. Li, L. L. Liu, and F. Martín, "Ultra-wideband and broad-angle linear polarization conversion metasurface," J. Appl. Phys. **121**, 174902 (2017).
24. B. Q. Lin, Y. X. Da, J. L. Wu, W. Li, Y. W. Fang, and Z. H. Zhu, "Ultra-wideband and high-efficiency cross polarization converter based on anisotropic metasurface," Microw. Opt. Technol. Lett. **58**, 2402–2405 (2016).
25. P. Zhou, F. Zhang, X. Ye, Q. Guo, and S. Pan, "Flexible frequency-hopping microwave generation by dynamic control of optically injected semiconductor laser," IEEE Photonics J. **8**, 5501909 (2017).
26. Z. Y. Song and J. H. Zhang, "Achieving broadband absorption and polarization conversion with a vanadium dioxide metasurface in the same terahertz frequencies," Opt. Express **28**, 12487–12497 (2020).
27. Z. Y. Song, Q. Q. Chu, X. P. Shen, and Q. H. Liu, "Wideband high-efficient linear polarization rotators," Front. Phys. **13**, 137803 (2018).
28. Z. Y. Song, L. Zhang, and Q. H. Liu, "High-efficiency broadband cross polarization converter for near-infrared light based on anisotropic plasmonic meta-surfaces," Plasmonics **11**, 61–64 (2016).

29. E. S. Montalvão, A. C. Montalvão, A. L. Campos, and A. G. Neto, "A new model of metasurface used for linear-to-circular polarization conversion in antenna array," Microw. Opt. Technol. Lett. **58**, 861–864 (2016).
30. E. Owiti, H. N. Yang, P. Liu, O. Calvine, and X. D. Sun, "Polarization converter with controllable birefringence based on hybrid all-dielectric-graphene metasurface," Nanoscale Res. Lett. **13**, 38 (2018).
31. S. Q. Chen, Y. B. Zhang, Z. Li, H. Cheng, and J. G. Tian, "Empowered layer effects and prominent properties in few-layer metasurfaces," Adv. Opt. Mater. **7**, 1801477 (2019).
32. C. C. Chang, Z. X. Zhao, D. F. Li, A. J. Taylor, S. H. Fan, and H. T. Chen, "Broadband linear-to-circular polarization conversion enabled by birefringent off-resonance reflective metasurfaces," Phys. Rev. Lett. **123**, 237401 (2019).
33. N. K. Grady, J. Z. Heyes, and D. R. Chowdhury, "Terahertz metamaterials for linear polarization conversion and anomalous refraction," Science **340**, 1304–1307 (2013).
34. X. Gao, X. Han, W. P. Cao, H. O. Li, H. F. Ma, and T. J. Cui, "Ultrawideband and high-effificiency linear polarization converter based on double V-shaped metasurface," IEEE Trans. Antennas Propag. **63**, 3522–3530 (2015).
35. F. Cong, Y. Z. Cheng, Z. Q. He, J. C. Zhao, and R. Z. Gong, "Design of a wideband reflective linear polarization converter based on the ladder-shaped structure metasurface," Optik **137**, 148–155 (2017).
36. Y. T. Jia, Y. Liu, W. B. Zhang, and S. X. Gong, "Ultra-wideband and high-efficiency polarization rotator based on metasurface," Appl. Phys. Lett. **109**, 051901 (2016).
37. J. C. Zhao, Y. Z. Cheng, and Z. Z. Cheng, "Design of a photo-excited switchable broadband reflective linear polarization conversion metasurface for terahertz waves," IEEE Photonics J. **10**, 4600210 (2018).
38. J. C. Zhao and Y. Z. Cheng, "Ultrathin dual-band polarization angle independent 90° polarization rotator with giant optical activity based on planar chiral metamaterial," Appl. Phys. B **124**, 185 (2018).
39. X. B. Liu, J. S. Zhang, W. Li, R. Lu, L. M. Li, Z. Xu, and A. X. Zhang, "Three-band polarization converter based on reflective metasurface," IEEE Antennas Wireless Propag. Lett. **16**, 924–927 (2016).
40. L. Zeng, H. F. Zhang, G. B. Liu, and T. Huang, "A three-dimensional linear-to-circular polarization converter tailored by the gravity field," Plasmonics **14**, 1347–1355 (2019).